Notice

This manuscript is a post-print uploaded to EarthArXiv. It has been peer-reviewed and published in GJI by Oxford University Press on behalf of The Royal Astronomical Society on 21/01/2019 with DOI 10.1093/gji/ggz041. The manuscript is also available via journal website.

Manuscript details

Title: 2-D P-SV and SH spectral element modelling of seismic wave propagation in non-linear media with pore-pressure effects
Authors: Elif ORAL (IRSN and IFSTTAR), Céline Gélis (IRSN), and Luis Fabian Bonilla (IFSTTAR)
Contact: elif.oral@geoazur.unice.fr

Geophysical Journal International

Geophys. J. Int. (2019) **217,** 1353–1365 doi: 10.1093/gji/ggz041
Advance Access publication 2019 January 21
GJI Seismology

2-D P-SV and SH spectral element modelling of seismic wave propagation in non-linear media with pore-pressure effects

Elif Oral,[1,2] Céline Gélis[1] and Luis Fabián Bonilla[2]

[1] *Institut de Radioprotection et de Sûreté Nucléaire, Fontenay-aux-Roses, France. E-mail: Elif.Oral@geoazur.unice.fr*
[2] *Institut Français des Sciences et Technologies des Transports, de l'Aménagement et des Réseaux, Marne-la-Vallée, France*

Accepted 2019 January 18. Received 2019 January 16; in original form 2018 July 16

Downloaded from https://academic.oup.com/gji/article-abstract/217/2/1353/5298487 by guest on 09 April 2019

SUMMARY

It has long been recognized that the effects of superficial geological layers, or site effects, can play a major role on the seismic ground motion at the free surface. In this study, we compute wave propagation in a 2-D asymmetrical basin considering both soil non-linearity and pore-pressure effects. Equations of elastodynamics of wave propagation are solved using the spectral element method (SEM). The geometry of the basin gives rise to basin-edge generated waves, that are different for in-plane (P-SV) and out-of-plane (SH) wave propagation and resulting in different non-linear response. Moreover, the excess-pore pressure development in superficial liquefiable layers (effective stress analysis) brings larger deformation and loss of strength than the analysis without pore-pressure effects (total stress analysis). The coupling of vertically propagating waves and the waves specifically generated in 1-D model leads to waves whose amplitude and duration are higher than the 1-D case. This multidimensional effect increases material non-linearity. Such complex wavefield provokes larger deformation and higher pore-pressure rise that cannot be predicted by 1-D modelling. Therefore, our paper suggests the use of multidimensional modelling while studying seismic wave propagation in both linear and non-linear complex media.

Key words: Elasticity and anelasticity; Numerical modelling; Earthquake ground motions; Site effects; Wave propagation.

1 INTRODUCTION

It is widely known that site effects play a major role on the amplification, duration and spatial variability of the earthquake ground motion. The destructive impact of site effects has been experienced by considerable human and material losses in past events such as the 1985 Michoacan, Mexico (Campillo *et al.* 1989), the 1995 Hyogoken-Nambu, Japan (Tokimatsu *et al.* 1996), the 1999 İzmit, Turkey (Bakir *et al.* 2002) and the 2015 Gorkha, Nepal (Chiaro *et al.* 2015) earthquakes. The nature and geometry of sedimentary structures may lead to strong diffraction of waves on curved boundaries and formation of basin-edge generated waves (Sanchez-Sesma *et al.* 1985; Kawase & Aki 1989; Chávez-García *et al.* 1994). Such an effect could further prolong the wave propagation and intensify the damage where waves pass through (Bard & Bouchon 1985). Therefore, the effect of multidimensional site geometry should be considered in site-specific studies.

In spite of the many observations worldwide, in order to understand the physical processes behind seismic wave propagation in complex media, numerical modelling is often needed. There are numerous studies of wave propagation that assume that the material behaves linearly (e.g. Olsen & Archuleta 1996; Delavaud 2007; Smerzini *et al.* 2011; Peyrusse *et al.* 2014). Yet, large ground motion could trigger material non-linearity, and if the sediments are water-saturated, pore-pressure effects may further modify the ground motion (i.e. Aguirre & Irikura 1997; Iai *et al.* 1995; Bonilla *et al.* 2005, 2011; Laurendeau *et al.* 2017). Significant spatial variability of ground motion can arise from excess-pore pressure development in presence of liquefiable soils as observed in the 2011 earthquake of Christchurch, New Zealand where widespread liquefaction was reported at different sites in the near field (Bradley & Cubrinovski 2011).

Conversely, relatively few studies focus on wave propagation in non-linear media. The 1-D analyses of Takemiya & Adam (1998) highlight the non-linearity effect on coastal zones during the 1995 Kobe earthquake by attenuation of ground acceleration for frequencies over 1 Hz. Roten *et al.* (2012) model the 3-D wave propagation in Wasatch Fault (USA) including 1-D soil non-linearity. They conclude that the calculated ground motion at near-source region gets closer to the prediction models only when high-frequency ground-motion damping due to soil non-linearity is accounted for. Other studies (Bonilla *et al.* 2006; Stupazzini *et al.* 2009; Gandomzadeh 2011; Martino *et al.* 2015) compare linear and non-linear approaches, revealing the significant attenuation of multidimensional basin response under high non-linearity. In some of these studies, the energy content of the modelled ground

© The Author(s) 2019. Published by Oxford University Press on behalf of The Royal Astronomical Society.

motion is shown to shift to lower frequencies than the natural frequency, and hence medium velocity is reduced and ground motion may last longer. Such non-linearity effects in multidimensional media have been shown to be strongly dependent on the complexity and the amplitude of the source (Gélis & Bonilla 2012, 2014). For example, Dupros *et al.* (2010) report that the increase of earthquake magnitude results in enhanced non-linearity and more permanent displacement in 3-D analyses of the French Riviera model.

Even though the importance of the effects of soil non-linearity and pore-pressure development on ground motion is generally acknowledged, to which extent these effects could control the surface motion in complex media has not yet been explicitly studied. A better understanding of this aspect is necessary to improve the interpretation of earthquake ground-motion recordings and hence to increase the quality of seismic hazard analyses. The objective of this paper is to study the effects of non-linearity on 1-D P-SV and SH wave propagation, with particular attention devoted to pore-pressure effects. For this purpose, we use the 1-D spectral element code SEM2DPACK (version 2.3.8; Ampuero 2002), which is available as open source code (detailed in Section 'Data and Resources'). This code has previously been used to model the dynamic rupture of non-planar faults and seismic wave radiation (Madariaga *et al.* 2006), fault reflections from fluid-infiltrated faults (Haney *et al.* 2007), non-linear wave propagation in damaged rocks (Lyakhovsky *et al.* 2009), wave propagation around a prototype nuclear waste storage tunnel (Smith & Snieder 2010) and benchmarks for wave propagation in heterogeneous media (O'Brien & Bean 2011). Within the scope of this study, we have implemented new features into SEM2DPACK to address the non-linear behaviour of surficial soil layers.

In Oral *et al.* (2017), we conducted 1-D three-component (3C) spectral element modelling of seismic wave propagation in non-linear media and performed validation tests of our approach through comparison with earthquake recordings on a liquefaction test site in California (Wildlife Refuge Liquefaction Array; WRLA). This work follows-up on Oral *et al.* (2017), extending the modelling to 1-D. Soil non-linearity is approximated by the Masing-Prager-Ishlinski-Iwan (MPII) rheology (Iwan 1967). MPII approach models material non-linearity by a set of nested yield surfaces consisting of linear elastic springs and Coulomb friction elements. As an input, it only requires the shear modulus reduction ratio as a function of shear strain, which is readily obtained from laboratory data or from the literature for a wide range of soil classes (Vucetic & Dobry 1991; EPRI 1993; Ishibashi & Zhang 1993; Darendeli 2001). Furthermore, we use the liquefaction front model of Iai *et al.* (1990) to take into account excess-pore pressure development in liquefiable soils. By doing so, we are able to model the sudden changes of dilatant/contractive behaviour of cohesionless soils due to cyclic mobility under undrained conditions. The liquefaction front model is based on an empirical relation that correlates pore-pressure changes to the shear work produced during wave propagation. It requires only few parameters that can be obtained from laboratory data or numerical analyses (Iai *et al.* 1990, 1995; Bonilla *et al.* 2005; Roten *et al.* 2013, 2014). For viscoelastic attenuation in the medium, the Liu & Archuleta (2006) model is used, which considers the total energy dissipation in viscoelastoplastic soil models calculated as the sum of viscoelastic attenuation and hysteretic attenuation (due to the strength weakening as a function of strain in the non-linear model) similarly to Assimaki *et al.* (2011), Gélis & Bonilla (2012, 2014) and Oral *et al.* (2017). The set of parameters required as model input comprises general physical soil properties (such as shear strength and liquefaction resistance). Therefore, the applicability of our numerical model is not merely limited to individual sites with precise data; the findings presented in this work are also helpful to understand and to reduce uncertainties in site-specific ground-motion assessments for other areas.

This paper is organized as follows. First, we briefly present the spectral element method and the constitutive material models. As a preliminary study, the viscoelastic basin response is computed for in-plane (P-SV) and out-of-plane (SH) wave propagation. Secondly, the non-linear response of a 1-D sedimentary basin model is analysed and compared to the viscoelastic case, and the effect of pore-pressure development on basin response is investigated through the comparison of different cases (non-linearity with/without pore-pressure effects). Differences between non-linear effects triggered in P-SV and SH models are pointed out. In the last section, differences in the non-linear basin response for the assumptions of 1-D and 1-D geometries are discussed. Finally, we offer perspectives and directives for future studies.

2 NUMERICAL SCHEME AND CONSTITUTIVE MODELS

The spectral element approximation is based on the decomposition of the domain into non-overlapping elements Ω_e (segments in 1-D, quadrangles in 1-D and hexahedra in 3-D). In each element Ω_e, Gauss–Lebatto–Legendre (GLL) integration points are defined. Lagrange polynomials are then chosen to define an orthogonal basis, which enables the SEM to have a spectral convergence, making it a very precise numerical method (Faccioli *et al.* 1997; Komatitsch & Vilotte 1998; Festa & Vilotte 2005; Delavaud 2007). In our case, the system of equation of wave propagation is expressed by velocity–stress formulation. The time discretization follows the leap-frog scheme. To ensure the stability of this time-marching solver, the time step has to satisfy the Courant–Friedrichs–Lewy (CFL) condition. Here the controlling value definition is adopted from Delavaud (2007), in which the computed CFL number is based on minimum spacing between GLL nodes of spectral element. To avoid artificial wave dispersion, the minimum element size $d_{\min}$ is constrained by the relation $d_{\min} \leq \lambda_{\min} N/ppw$, where $\lambda_{\min}$ is the shortest wavelength propagating in the medium, N is the polynomial degree and ppw is the number of grid points per wavelength (Seriani & Priolo 1991, 1993). We use 0.3 as the controlling value of CFL and set 5 GLL points (corresponding to a 4th polynomial degree) for $ppw = 5$ for all the applications in this paper.

The propagation of pressure (P) and shear (S) waves in a 1-D vertical plane can be defined in two ways in SEM2DPACK by considering (1) only in-plane P waves and the vertical component of S waves (SV), or (2) only the out-of-plane, horizontal component of S waves (SH). For the remainder of this paper, P-SV and SH models denote the first and second case, respectively. For P-SV waves, the elastodynamic equation of wave motion is written in a vertical plane (x, z) in terms of horizontal and vertical partial terms of external force (f_x and f_z for horizontal and vertical directions, respectively), stress tensor σ ($\sigma_{xx}, \sigma_{zz}, \sigma_{xz}$) and time derivatives of velocity (v_x and v_z for horizontal and vertical directions, respectively) as follows:

$$\rho \frac{\partial v_x}{\partial t} = \left(\frac{\partial \sigma_{xx}}{\partial x} + \frac{\partial \sigma_{xz}}{\partial z} \right) + f_x \tag{1}$$

$$\rho \frac{\partial v_z}{\partial t} = \left(\frac{\partial \sigma_{zz}}{\partial z} + \frac{\partial \sigma_{xz}}{\partial x} \right) + f_z. \tag{2}$$

Downloaded from https://academic.oup.com/gji/article-abstract/217/2/1353/5298487 by guest on 09 April 2019

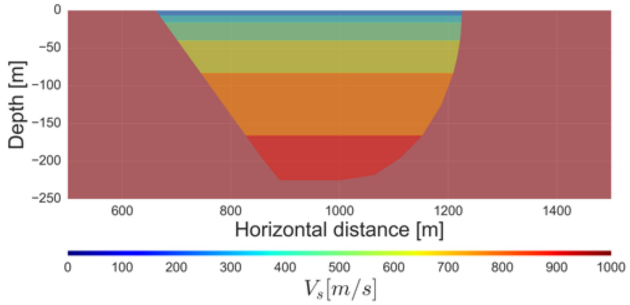

Figure 1. Shear wave velocity profile of the 1-D sedimentary basin model. The bedrock shear wave velocity is 2000 m s^{-1}.

For SH waves, the elastodynamic equation of wave motion is expressed as:

$$\rho \frac{\partial v_y}{\partial t} = \left(\frac{\partial \sigma_{xy}}{\partial x} + \frac{\partial \sigma_{yz}}{\partial z} \right) + f_y, \tag{3}$$

where v_y is the out-of-plane (x, z) velocity field, and f_y is the force acting in the same direction as v_y.

We implement different soil constitutive models into the 1-D SEM scheme. MPII non-linear constitutive model of Iwan (1967) is used following the implementation of Joyner (1975). In Oral *et al.* (2017), the implemented MPII model holds for 3-D soil non-linearity and only non-zero components are used for 1-D wave propagation. We use the same formulation for the 3-D soil non-linearity model. Non-zero components are determined with respect to the P-SV or SH wave propagation model. The shear modulus degradation is approximated by the hyperbolic model proposed by Hardin & Drnevich (1972). Eq. (4) shows the relation between shear modulus G and shear strain γ for this model, where G_0 is the elastic shear modulus and γ_{ref} is the reference shear strain defined as the ratio between the shear strength and the elastic shear modulus:

$$\frac{G}{G_0} = \frac{1}{1 + \gamma/\gamma_{\mathrm{ref}}}. \tag{4}$$

The liquefaction front model of Iai *et al.* (1990) is implemented for modelling pore-pressure effects. A detailed explanation about the coupling of MPII model and the liquefaction front model is given in Pham (2013) & Oral (2016). At each time step of the simulation, shear modulus and reference strain are calculated based on the current pore-pressure rise. Then, an updated characteristic backbone curve is constructed accounting for the current values of parameters of MPII model. Verification of the implementation of the viscoelastic and non-linear constitutive models based on comparison of 1-D and 1-D models is detailed in Supplementary Appendix A (supplementary material is available to download with the online version of the paper).

3 NON-LINEAR RESPONSE OF A 1-D SEDIMENTARY BASIN MODEL

3.1 Basin properties

We use the same 1-D basin model as in Gélis & Bonilla (2014). The model domain has a length of 2000 m and a depth of 250 m, Fig. 1. The sedimentary basin has a depth of 225 m and it is surrounded by bedrock. The basin width varies from 563 m at the surface to 110 m at the base. The left boundary is represented by a straight slope that gives rise to sharp changes along this basin edge, most notably close to the surface. The basin has an elliptic shape at its right boundary. Such an asymmetrical shape was proposed by Lacave & Lemeille (2006) to describe the general shape of Alpine valleys.

The model further consists of six soft layers inside the sedimentary basin. Shear velocity increases gradually towards the bottom of the basin. In Gélis & Bonilla (2014), two different velocity models are compared to assess the influence of the velocity distribution on the basin response. In the first model, velocity gradually changes within a soil layer, so that each point at a given depth is defined by a different velocity. In the second model, the basin is divided into layers of constant velocity, which are derived from the velocities of the first model. In their study, the basin response at the surface is shown to be weakly sensitive to constant versus gradually increasing velocities in each layer, as compared to the effect of the soil constitutive model. For convenience, we assume homogeneous soil layers in terms of shear velocity profile in our 1-D model.

To determine whether the seismic behaviour of our basin model is close to 1-D or 1-D in terms of resonance pattern, simple considerations of the basin properties (basin geometry and velocity contrast between the sedimentary layers and the bedrock) can give first indications. In Bard & Bouchon (1985), the nature of specific resonance patterns in 1-D sedimentary deposits is investigated for a homogeneous and sinusoidal-shaped basin. 1-D resonance produces considerably larger amplifications and longer duration of propagation compared to 1-D. The authors have shown that the existence of resonance modes (for P, SV and SH waves) in 1-D models is strongly dependent on the shape ratio (ratio of basin depth and width) and velocity contrast with respect to the bedrock. In shallow earth structures, laterally propagating surface waves dominate the ground motion and locally 1-D resonances may occur at bedrock/sediment interfaces. In deeper structures, 1-D resonance pattern is expected due to the interference of surface waves and vertically propagating waves. In Bard & Bouchon (1985), a curve constrained by the basin properties separates the 1-D resonance and lateral propagation of surface waves from the 1-D-resonance regime for SH wave propagation. By calculating the shape ratio (0.79) and minimum and maximum velocity contrasts (2.2 and 7.1, respectively) of our basin model, the resultant point remains inside the 1-D-resonance regime for both lower and upper limits of the velocity contrasts. Such a result indicates that SH wave propagation in our 1-D model should be dominated by the 1-D resonance mode of the basin.

Gélis & Bonilla (2012) demonstrated the strong dependence of the basin response on the soil constitutive model by comparing viscoelastic and viscoelastoplastic models exhibiting various degrees of amplitude and complexity of input motion. In their study, the non-linear soil model was taken to be independent of pressure, and non-linear curves from EPRI (1993) with different level of non-linearity were adopted for each layer in the basin. In our study, we consider pressure-dependent soil properties so that non-linearity changes with depth within a given layer (owing to the effect of confining stress). Non-linearity parameters of GLL points on a spectral element depend on the depth of the point. Thus, the initial shear modulus of each GLL point is multiplied by a coefficient of $(\frac{\sigma'}{\sigma'_{mid}})^{0.5}$, where σ' is the initial effective stress at the point and σ'_{mid} is the effective confining stress at mid-layer. The water table is set to GL-2 m and is located inside the first layer. Although water table depth is likely to differ horizontally in reality, in this paper, we consider a water table level that is spatially uniform.

Downloaded from https://academic.oup.com/gji/article-abstract/217/2/1353/5298487 by guest on 09 April 2019

The values of shear and pressure wave velocities (V_s and V_p), mass density ρ, quality factors for pressure and shear wave propagation Q_p and Q_s, reference frequency and thickness are taken from Gélis & Bonilla (2014), Table 1.

We suppose that the first two layers are capable of generating pore-pressure excess. We also suppose that the medium composition is identical, with the distinction made only through the *P*- and *S*-wave velocities. Such a configuration implies that the two layers exhibit identical plastic features (i.e. friction and phase transformation angle, and dilatancy parameters; see Table 2). Failure line angle ϕ_f is greater for deeper soils as confining pressures at mid-layer σ'_{mid} increases with depth. Also, the coefficient of Earth at rest is set to 1, such that the initial consolidation is isotropic.

The liquefaction susceptibility is represented by the liquefaction resistance curve. This curve is determined by a series of stress-controlled experimental/numerical experiments. In these tests, soil is loaded under different cyclic stress ratios (CSR, defined as the ratio of applied deviatoric stress to effective mean stress). The liquefaction limit is defined as the number of loading cycles triggering 5 per cent peak-to-peak of shear strain (corresponding to an axial strain of 2.5 per cent). The liquefaction resistance curve for a layer is constructed by assembling the number of loading cycles which are calculated for different applied cyclic stress ratios in the numerical tests. One example of such numerical stress-controlled tests is detailed in Appendix B1.

Following Iai *et al.* (1995), we build a liquefaction curve for the liquefiable layers of our model. Non-linearity parameters are obtained from a trial-and-error procedure constraining these liquefaction curve, and are listed in Table 2. The number of loading cycles triggering 5 per cent of shear strain under four different levels of loading (cyclic stress ratio) are plotted in Fig. 2. The initial effective mean stress is calculated as 47.040 and 109.760 kPa at the mid-layer depths of layer 1 and 2, respectively. As seen in this figure, 12 loading cycles are required to initiate liquefaction in layer 1 for a stress ratio of 0.17, whereas approximately 4 cycles are necessary for a stress ratio of 0.24. Comparing the two curves, layer 1 liquefies after being subjected to fewer loading cycles than layer 2 for a given CSR.

3.2 Numerical model

Since the soil non-linearity is taken into account in the analyses of this paper, the medium has to be spatially oversampled compared to the linear case. Following Gélis & Bonilla (2012, 2014) and Oral *et al.* (2017), we first assume that the minimum shear velocity does not decrease to a value less than one-fourth of the initial shear velocity, and then verify that this assumption is valid at the end of the simulation.

For the lateral boundaries of the simulation domain, periodic boundary conditions were adopted. The upper boundary is set to a free surface. An absorbing boundary condition (following the P1 approximation of Stacey 1988) is adopted for the bottom boundary at GL-250 m. The incident wavefield is inserted at this depth, and all vertically downgoing waves are absorbed (Delavaud *et al.* 2006). Through additional tests performed on linear and non-linear cases, we verified that no undesired reflections (with the potential to significantly change the results) are generated as a result of the prescribed absorbing boundary condition, and that no energy is supplemented to the medium through the periodic boundaries.

As an input motion, a truncated Gaussian synthetic signal is taken as input motion. This signal was provided by the E2VP benchmark of the EUROSEISTEST project material (Mauffroy *et al.* 2015), which has the benefit of being short in time (impulsive) while exhibiting a broad-band frequency content. The acceleration-time history and the corresponding Fourier amplitude are shown in Fig. 3. The PGA of the incident wavefield corresponds to 0.1 g (before filtering is applied; it approximately equals 0.075 g after filtering), and hence, 0.2 g at the free surface. The signal is filtered on the frequency band of 0.2–10 Hz by a Butterworth filter. The duration of all of the simulations is set to 7 s with a time step of 2×10^{-5} s.

3.3 Results

3.3.1 Viscoelastic response of the 1-D basin model

Viscoelasticity is defined to be pressure dependent in our model, so that the soil properties in a spectral element depend on the confining pressure applied at its depth. The solution of the viscoelastic case is taken as a reference case in the discussion of the basin response in the presence of non-linear soil. The verification of the viscoelasticity model for the 1-D basin model is provided in Appendix A together with the verifications of the implementation of other constitutive models in SEM2DPACK. First, we analyse the velocity-time histories recorded at the free surface. Fig. 4 displays the velocity wavefield of the horizontal components at the free surface of the P-SV model (top panel) and the SH model (bottom panel). The seismic stations are situated between 500 and 1500 m from the left boundary with a spacing of 10 m. The influence of the basin asymmetry on both models is apparent from the greater angle of wave reflection at the left side of the basin after the arrival of the first waves (after 1.5 s). Then, strong reflection of waves travelling across the basin width continues during roughly 4 s in both models. Wave propagation generated at the basin margins after 3 s is more pronounced in the SH model than in the P-SV model. Attenuation of basin waves occurs within 2 s for the two models, while this duration is 0.5 s in the bedrock.

In addition to the particle velocities, the spectral ratios are computed for the P-SV and SH wave propagation, Fig. 5. The spectral ratios are computed as the ratio of FFT values of basin signals to the geometric mean of bedrock signals. The fundamental frequency corresponds to 1.25 Hz and 1 Hz for P-SV and SH wave propagation, respectively. The influence of the basin asymmetry on the P-SV wave propagation is evident from the spectral ratio values, which are higher close to the right basin boundary than to the left boundary. To a lesser extent, this asymmetric amplification is also apparent for the SH case.

We recall that the 1-D resonance pattern is expected to dominate the SH wave propagation, as suggested by Bard & Bouchon (1985). To compare 1-D and 1-D natural frequencies, we computed the mean shear-wave velocity of basin soil, using the traveltime-based shear-wave velocity average as proposed by Roten *et al.* (2006). This value equals to 642.8 m s^{-1} and corresponds to a 1-D fundamental frequency of 0.7 Hz. The calculated 1-D fundamental resonance frequencies are notably greater than the 1-D frequencies (greater by a factor 1.8 for SV waves and 1.4 for SH waves). This difference between 1-D and 1-D natural frequencies underlines the importance of the geometry effect on the basin response for both P-SV and SH wave propagation.

Downloaded from https://academic.oup.com/gji/article-abstract/217/2/1353/5298487 by guest on 09 April 2019

Table 1. Soil properties of the 1-D basin model (after Gélis & Bonilla 2014).

Layer	V_s (m s^{-1})	V_p (m s^{-1})	ρ (kg m^{-3})	Q_s	Q_p
1	278.5	923.7	1800	20	40
2	362.4	1202.0	1800	20	40
3	456.9	1515.4	1800	20	40
4	585.2	1940.9	1800	20	40
5	749.8	2486.8	1800	20	40
6	897.5	2976.7	1800	20	40
Bedrock	2000.0	4163.3	2200	100	200

Table 2. Consolidation properties and dilatancy parameters for the 1-D model.

Layer	Depth range (m)	ϕ_f (°)	σ'_{mid} (kPa)	ϕ_p (°)	w_1	p_1	p_2	S_1
1	0–7	35	47.040	24	5.0	0.6	1.2	0.01
2	7–16	35	109.760	24	5.0	0.6	1.2	0.01
3	16–40	38	239.120	–	–	–	–	–
4	40–83	38	501.760	–	–	–	–	–
5	83–166	40	995.680	–	–	–	–	–
6	166–225	40	1552.320	–	–	–	–	–

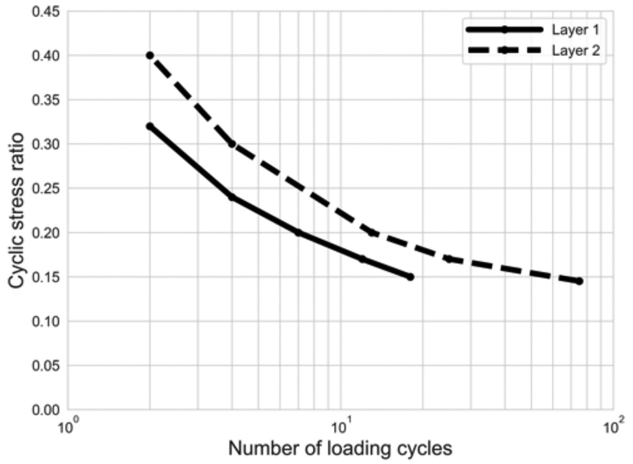

Figure 2. Liquefaction resistance curves for layer 1 (dashed line) and layer 2 (solid line) of the 1-D model.

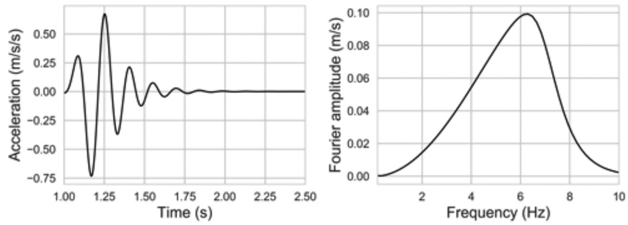

Figure 3. Acceleration-time histories (left-hand panel) and Fourier amplitude (right-hand panel) of the input signal.

Moreover, Bard & Bouchon (1985) demonstrated that SV waves resonate at higher frequencies than SH waves by a certain factor depending on the shape ratio of the propagation medium. In our case, the fundamental frequency for SH wave propagation is smaller than for the P-SV case, in accordance with Bard & Bouchon (1985). As a result, the distribution of spectral ratios within the basin is different for the two cases: amplifications globally appear at lower frequencies in the SH case than in the P-SV case. Slight amplifications are noted close to the right boundary for the frequencies above 2 Hz. Since the SH waves are out-of-plane and P-SV waves are in-plane,

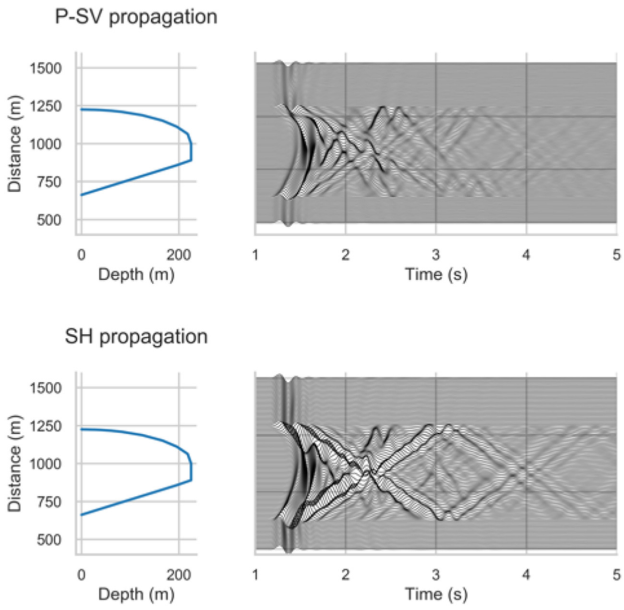

Figure 4. Horizontal components of the particle velocity at the free surface of the P-SV model (top panel) and SH model (bottom panel) for viscoelastic wave propagation in the 1-D basin model subject to an input motion of PGA 0.2 g. For reference, the profile of the basin is plotted (sideways) in the left-hand panels.

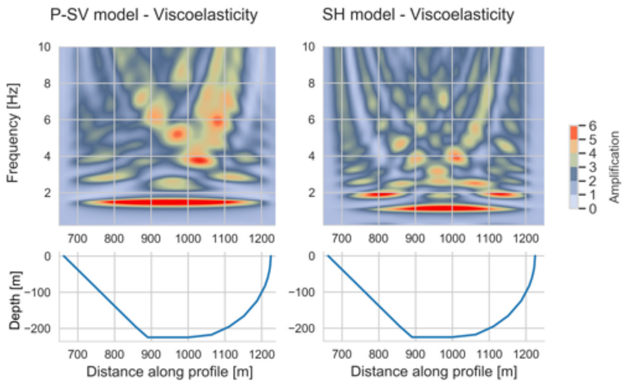

Figure 5. Spectral-ratio distribution of the viscoelastic surface motion for horizontal component of P-SV model (left-hand panel) and SH model (right-hand panel) on the frequency band 0.2–10 Hz. For reference, the profile of the basin is plotted in the lower panels.

Downloaded from https://academic.oup.com/gji/article-abstract/217/2/1353/5298487 by guest on 09 April 2019

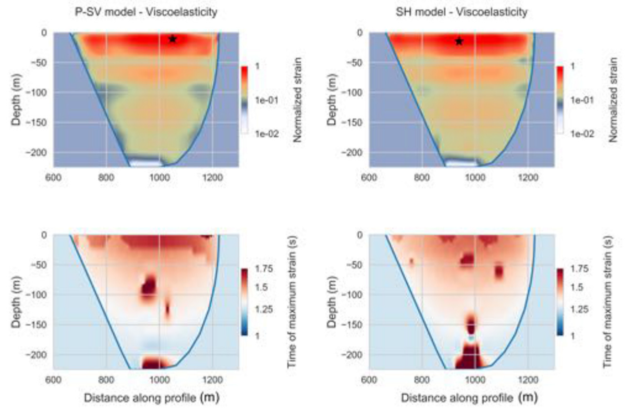

Figure 6. Maximum-strain (top panels) and trigger-time (bottom panels) distribution of the P-SV model (left-hand panels) and the SH model (right-hand panels) for viscoelasticity. The locations of maximum strain values are indicated by a star.

the reflections inside the basin are expected to be differently influenced by the basin geometry. Such a difference in wave propagation could explain the differences in the distribution of P-SV and SH models.

It is also known that the impedance contrast inside the basin can affect the resonance modes of SV and SH waves (Semblat *et al.* 2005; Ermert *et al.* 2014). To distinguish the effect of the impedance contrast from that of the basin geometry, we performed additional analyses (not shown here), where we simulated P-SV and SH wave propagation by assuming a single type of sedimentary soil inside basin. The shear wave velocity was set to the mean shear velocity of the basin soil (642.8 m s^{-1} as aforementioned). The analyses showed that the homogeneous basin resonates at approximately 1.5 Hz and 1 Hz for P-SV and SH cases, respectively. The difference between the 1-D (being 0.7 Hz) and 1-D natural frequencies also persisted for homogeneous basin simulations, which highlights the importance of the effect of 1-D geometry on P-SV and SH basin responses.

To investigate the ultimate deformation reached in the basin for each case (P-SV and SH models), we analyse the maximum shear strain, Fig. 6 (top panels). This figure presents the maximum shear strain values normalized by the maximum value of shear strain of the P-SV model for each point of the basin. The maximum strain value over the entire basin is 0.022 per cent for the P-SV model, and it is slightly lower in the SH model (0.019 per cent). The highest values are concentrated in the upper layers down to GL-50 m. The location where the maximum strain is calculated is marked by a star. This location is different for the P-SV and SH models: in the P-SV model it is close to the right boundary ($x = 1050$ m) at GL-11.5 m, while in the SH model it is close to the centre ($x = 940$ m) at GL-15 m. The values of maximum strain decrease for deeper layers in both models, and layering of maximum-strain patches is clearly seen. The presence of such discrete regions of strain inside the sediment layers can be attributed to the velocity contrast between each subsequent layer. Higher strain values are calculated close to layer boundaries. Such layering was also obtained by Gélis & Bonilla (2014), who showed that a gradually increasing velocity profile produces a slightly smoother strain distribution. A similar result of elevated strain values at layer boundaries was also reported by Gandomzadeh (2011) for a 1-D non-linear model of the Nice basin (France).

The instant at which the maximum strain is reached is also computed (bottom panels of Fig. 6). In both models, the maximum-strain values in superficial layers are generally reached before 1.75 s. This indicates that the highest strain values in upper layers are triggered by the incidence of the strongest part of the input motion (between 1 and 1.5 s as shown in Fig. 4). Incident waves reflected back from the free surface towards the basin bottom (after 1.75 s) increase the degree of deformation reached at the bottom of the basin near the bedrock interface, even though the maximum strain in these layers is relatively low. We observe an overall tendency of the strain to increase towards the surface, and that the high values of strain result from the strongest part of the incident waves inside the basin.

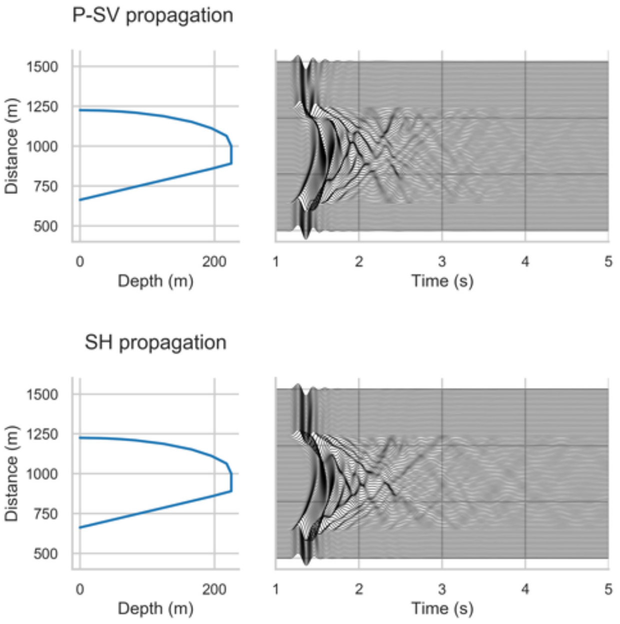

Figure 7. Horizontal components of the particle velocity at the free surface of the P-SV model (top panel) and SH model (bottom panel) for the non-linear model without pore-pressure effects in the 1-D basin model in response to the input motion of PGA 0.2 g. For reference, the profile of the basin is plotted (sideways) in the left-hand panels.

3.3.2 Non-linear response of the 1-D basin model

We analyse the non-linear response of the basin with and without consideration of excess-pore pressure development for P-SV and SH wave propagation types. The input motion is the same as in the viscoelastic case (Fig. 3). First, we analyse the non-linear surface motion in the P-SV and SH models. Fig. 7 shows the wavefield velocity of the horizontal components at the free surface of the P-SV model (top panel) and the SH model (bottom panel) for the non-linear soil response with no pore-pressure effects. The amplitude of the basin waves is strongly attenuated in both models due to non-linearity. The propagation of the basin waves travelling from one basin margin to the other is attenuated. The strongest part of the input motion is present in the beginning of the signal. Hence, the non-linearity-related effects are triggered from the beginning of propagation. However, the energy content of realistic input motions is rather complex in both the time and frequency domains (Gélis & Bonilla 2012), and the strongest part of the ground motion does not correspond to first arrivals. Such complexity of input motion may exert different controls on ground motion by continuous changes in loading/unloading cycles. We reserve this aspect for future studies. Instead, we concentrate on the effect of the non-linear response on

Downloaded from https://academic.oup.com/gji/article-abstract/217/2/1353/5298487 by guest on 09 April 2019

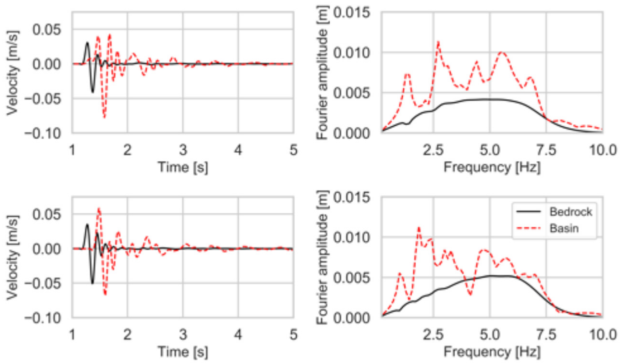

Figure 8. Velocity-time histories (left-hand panels) and Fourier amplitude (right-hand panels) of the bedrock (solid black lines) and the basin (dashed red lines) for the non-linear model without pore-pressure effects (total stress analysis) of P-SV (top panels) and SH (bottom panels) propagation models.

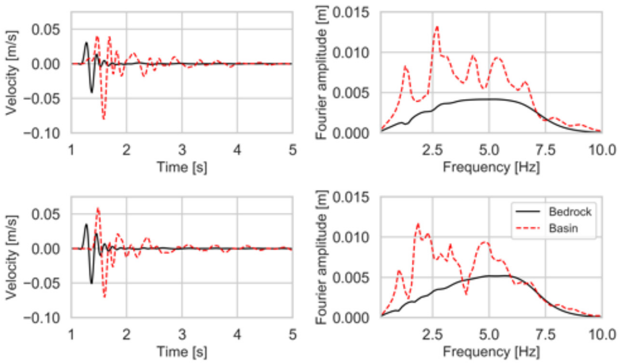

Figure 9. Velocity-time histories (left-hand panels) and Fourier amplitude (right-hand panels) of the bedrock (solid black lines) and the basin (dashed red lines) for the non-linear model with pore-pressure effects (effective stress analysis) of P-SV (top panels) and SH (bottom panels) propagation models.

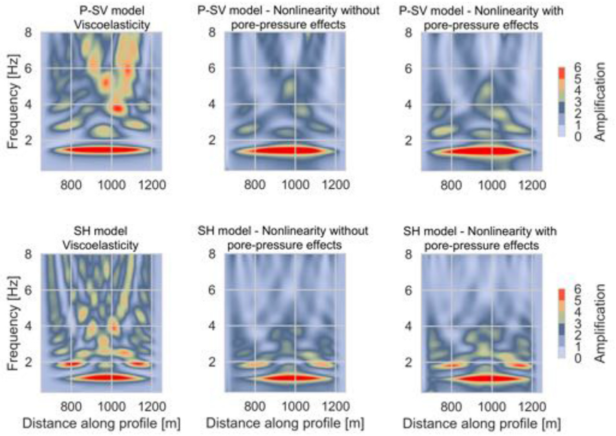

Figure 10. Spectral-ratio distribution of the surface-motion for the horizontal component of the P-SV model (top panels) and SH model (bottom panels) for the viscoelastic model (left-hand panels), the non-linear model without pore-pressure effects (total stress analysis; middle panels), and the non-linear model with pore-pressure effects (effective stress analysis; right-hand panels).

wave propagation, which warrants the use of a simple signal to isolate this phenomenon.

We compare velocity–time histories and their Fourier amplitude at the basin and bedrock surface for the P-SV and SH models. The basin signal is chosen at a position of $x = 1100$ m from the left boundary, and the bedrock signal is represented by the geometric mean of all bedrock stations (Fig. 8). We first make the comparison for the non-linear basin in the absence of pore-pressure effects. The waves refracted from the basin into the bedrock are different in the P-SV and SH cases, and therefore slight amplification in the wave and Fourier amplitudes in the bedrock (black lines) is observed in the SH model as compared to the P-SV model. Similar to the linear case, the amplitudes of both the P-SV and SH basin waves are greater than those of bedrock, and the duration of propagation is longer inside the basin. Waves are amplified in the whole frequency band inside the basin, and the waveform and energy content of P-SV and SH waves inside the basin are different. Recall that P-SV and SH wave propagation of the vertically incident horizontal wavefield would be identical in a medium where no horizontal variation of soil layer exists. Here the 1-D basin shape promotes differences in P-SV and SH wave propagation, since the formation of P waves due to the basin geometry is not present in the SH model. We also note that the Fourier amplitude of the calculated ground motion of both the basin and bedrock decreases beyond 8 Hz, reflecting the limited energy contained in the source.

Next, we make a comparison between the surface motion of the basin and bedrock for non-linearity with pore-pressure effects. Again both the P-SV and SH models are analysed (Fig. 9). The waveform and spectral shape of the non-linear basin response is preserved also under the effect of excess-pore pressure development for both the P-SV and SH models. Slight changes in velocity amplitudes and the peaks of Fourier amplitudes are observed as a result of pore-pressure effects.

Previous studies (e.g. Roten *et al.* 2012; Martino *et al.* 2015) have demonstrated that soil non-linearity influences wave propagation by signal damping, particularly at high frequencies, and causes a shift in resonance frequencies towards lower values. In Gélis & Bonilla (2014), such non-linearity effects are shown to be dependent on the spectral content of the input signal. In their study, a global diminution of spectral-ratio amplitudes is observed when the basin is affected by non-linear effects even under a simple impulse Gabor signal. In the same study, the non-linear basin response under a real input motion exhibits an amplified high-frequency content. Such an amplification has been attributed to the low values of Fourier amplitudes at the corresponding frequencies. Here, the energy content of the source is relatively weak at high frequencies (>8 Hz), as compared to the rest of the frequency band. Thus, the following analyses are performed up to 8 Hz where the source energy is sufficiently high.

To compare the spectral-ratio amplitudes at the whole basin surface for the viscoelastic and non-linear propagation media, we analyse transfer functions. Fig. 10 shows this comparison for viscoelasticity (left) and non-linearity without pore-pressure effects (total stress analysis; middle). We note that the basin non-linearity without pore-pressure effects results in attenuation of spectral ratios at intermediate frequencies (>2 Hz) in both P-SV and SH models. The natural frequency of the basin is shifted slightly to lower values compared to viscoelasticity: it is reduced from 1.25 to 1.15 Hz for the P-SV case and from 1 to 0.85 Hz for the SH model, respectively. It is worth noting that the distribution of the non-linear P-SV and SH models are still similar to the viscoelastic models.

To analyse the effect of excess-pore pressure development on the basin response, the transfer function for non-linearity with pore-pressure effects (effective stress analysis) is also computed (right-hand panels in Fig. 10). Compared to the total stress analysis, a

Downloaded from https://academic.oup.com/gji/article-abstract/217/2/1353/5298487 by guest on 09 April 2019

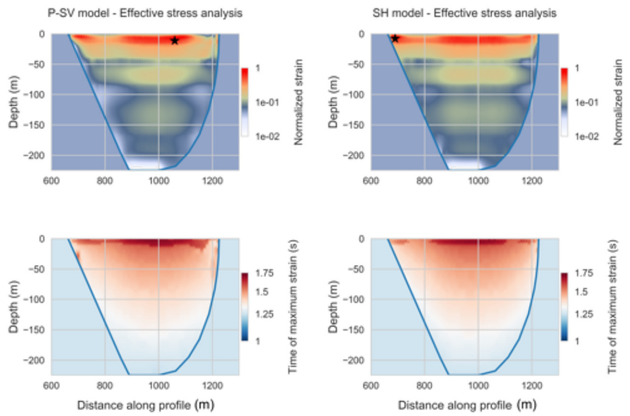

Figure 11. Maximum-strain (top panels) and trigger-time (bottom panels) distribution of the P-SV model (left-hand panels) and SH model (right-hand panels) for non-linearity with pore-pressure effects. The locations of the maximum-strain values are indicated by a star.

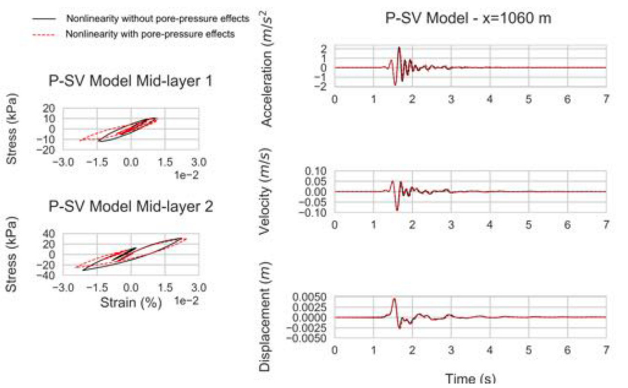

Figure 12. Comparison of stress–strain curves (left-hand panel) at GL-3.5 m (top panels) and GL-11.5 m (bottom panels) and comparison of time histories (right-hand panel) of surface-acceleration (top panel), velocity (middle panel) and displacement (bottom panel) between effective (dashed lines) and total (solid lines) stress analyses in the P-SV model.

slight influence attributed to pore-pressure effects is observed in the amplification of spectral ratios at low frequencies (<4 Hz), which is mostly pronounced at the basin margins. At high frequencies (>4 Hz), pore-pressure effects cause damping of the ground motion as compared to the total stress analysis.

Like in the total stress analysis, we inspect the distribution of the maximum strain achieved in the basin for the P-SV and SH models in the effective stress analysis, for which the triggered non-linearity level is higher due to pore-pressure effects. Fig. 11 (top panels) displays the maximum-strain distributions in the basin for the P-SV (top panel) and SH (bottom panel) models. As before, the strain values are normalized by the maximum value of the SH model. The maximum strain value over the entire basin is 0.045 per cent for the SH model, and it is marginally higher than for the P-SV model (0.044 per cent). These values are approximately twice that of the viscoelastic case. Maximum deformation in viscoelastic case is reached for the P-SV case, whereas it is reached for the SH model in non-linear case. By contrast, the differences between the two non-linear models (P-SV and SH models) are minor. The highest values of strain are concentrated in highly superficial layers where the soil is the most non-linear and excess-pore pressure development occurs. In particular, the central part of the basin and the basin margins experience higher strains than the rest of the basin. Although the maximum strain values of P-SV and SH models are close, the location of these points is different similar to the viscoelastic case: It remains in the centre of the basin for the P-SV model ($x = 1060$ m) at GL-6 m and is shifted towards the left margin of the basin in the SH model ($x = 690$ m) at GL-6 m. Further analysis reveals that the maximum strain of the non-linear basin without pore-pressure effects equals roughly 0.024 per cent for both the P-SV and SH models, being very close to the viscoelastic case, and also its lateral position is the same as in the viscoelastic case. However, this location is shifted to shallower depths due to non-linearity (from GL-8 m to GL-6 m for the P-SV case and from GL-11.5 m to GL-6 m for the SH case). Such a shift effect is also noted under pore-pressure effects: as the basin becomes more non-linear, the location of maximum strain is shifted further to shallower depths.

Regarding the triggering-time distribution of the maximum-strain values (bottom panels in Fig. 11), the basin becomes non-linear within 1.5 s. Similarly to the viscoelastic case, the maximum deformation is attributed to the strongest ground motion for superficial layers. Yet, small patches of maximum strain induced by later wave arrivals, as seen in the viscoelastic case, are not present here. Furthermore, we verified that the triggering-time distribution of maximum-strain values is very similar for both non-linearity cases with and without pore-pressure effects. Thus, the absence of small patches of enhanced deformation could be related to the damping caused by non-linearity.

Gélis & Bonilla (2014) concluded that maximum shear strain reaches higher values in superficial layers than in underlying layers. This localization effect is even more pronounced in this study, owing to the pressure dependency of non-linearity and the pore-pressure effects which reduce the soil strength near the surface. Because of the same effects, the contrast between the strain level in the various basin layers is enhanced compared to the viscoelastic case. We also observe higher strain values close to the basin margins, in particular close to the left boundary that is more steeply inclined than the right boundary. Such a finding is in agreement with Guidotti *et al.* (2011) who considered different combinations of model geometry and material properties in 1-D trapezoidal models, subjected to vertically propagating SV waves. They showed that the 1-D non-linear valley response is highly dependent on the basin geometry, and it is mostly pronounced close to the basin margins.

Next, we analyse the differences between total and effective stress computations by displaying the stress–strain curves, for both P-SV and SH cases with and without pore-pressure effects (left-hand panels in Fig. 12. The stress–strain curves are obtained from the middle of the first layer (top panel) and the middle of the second layer (bottom panel) at the centre of the basin at $x = 1060$ m, where strong non-linear effects have been computed (Fig. 11). Comparison of stress–strain curves between the simulations with and without pore-pressure effects reveals similar resultant behaviour in layer 1 and layer 2. In both layers, increased non-linearity level due to pore-pressure effects causes strain increase and strength weakening as the shear modulus (slope of stress–strain curve) is lowered owing to the rise of pore-pressure excess. The difference between total and effective stress analyses is more pronounced for layer 1. The triggered non-linearity is comparatively small, taking into account that the maximum deformation is less than 0.1 per cent, and only minor differences in stress–strain curves result from pore-pressure effects.

Downloaded from https://academic.oup.com/gji/article-abstract/217/2/1353/5298487 by guest on 09 April 2019

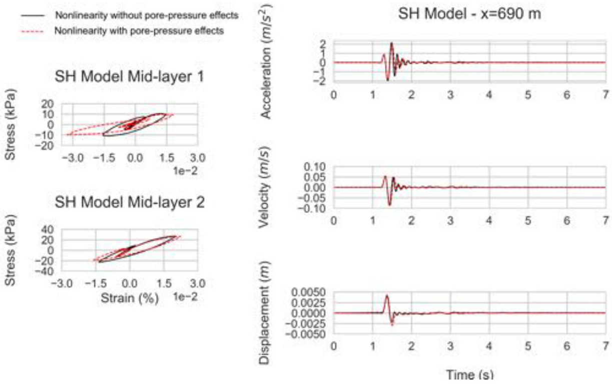

Figure 13. Comparison of stress–strain curves (left-hand panels) at GL-3.5 m (top panel) and GL-11.5 m (bottom panel) and comparison of time histories (right-hand panels) of surface-acceleration (top panel), velocity (middle panel), and displacement (bottom panel) between effective (dashed lines) and total (solid lines) stress analyses in the SH model.

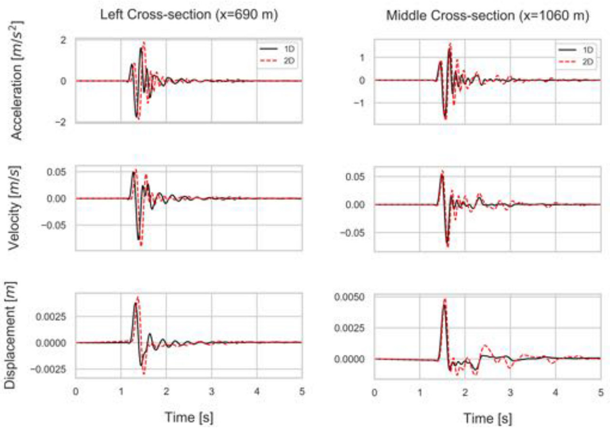

Figure 14. Comparison of time histories of surface acceleration (top panel), velocity (middle panel) and displacement (bottom panel) between 1-D (solid lines) and 1-D (dashed lines) approaches for the left column (left-hand panel) and central column (right-hand panel) for non-linearity with pore-pressure effects.

The same comparison as for the P-SV model is presented in Fig. 13 for the SH model. The stress–strain data are obtained from the top two layers at a point located in the left section of the basin at $x = 690$ m, where the highest strain is computed. Similar to the P-SV model, pore-pressure effects manifest themselves in elevated strain and in strength loss, which is particularly apparent in the first layer. Owing to the higher degree of non-linearity compared to the P-SV model, the maximum strain values are greater in the SH model than in the P-SV model (for example, 0.023 per cent in P-SV model and 0.035 per cent in SH model for layer 1). However, these differences are rather small given the limited degree of triggered non-linearity.

Surface-acceleration, velocity, and displacement time histories for the total and effective stress analyses of P-SV and SH models are also compared, as presented in the right panels of Figs 12 and 13, respectively. Waveforms of the P-SV and SH models diverge after 1.5 s: amplitudes of oscillations are amplified in the P-SV model compared to the SH model. This is similarly seen in the results of the two models when considering the differences between the total and effective stress analyses. Pore-pressure effects lead to slight damping in amplitude before 2 s, and waves exhibit a slight phase shift. Peak ground acceleration (PGA) is approximately 2 m s^{-2}, peak ground velocity (PGV) is 0.095 m s^{-1}, and maximum displacement is 0.48 cm for both approaches. Similar to the stress–strain curves, pore-pressure effects on surface-motion time histories are not substantial either. Such an outcome could be attributed to the small degree of deformation that the soil experiences under the imposed loading condition, acknowledging the simplicity of the input motion in terms of its loading/unloading history.

We also verified that these findings (non-linear effects in P-SV and SH models) are stable after changing liquefaction-related parameters for the first two layers. Details of this analysis can be found in Supplementary Appendix B2.

3.3.3 Comparison of non-linear basin response of 1-D and 1-D approaches

In the following section, we explore the effect of 2-D structure of the basin on soil non-linearity by comparing 1-D and 1-D model results for two different locations within the basin, adopting the non-linear soil constitutive model with pore-pressure effects. Results are shown for the SH model since the observed basin non-linearity is higher for the SH model than for the P-SV model. We perform the simulations with the 1-D-3C SEM code of Oral *et al.* (2017) for 1-D modelling using the 1-D soil properties at the left ($x = 690$ m) and central ($x = 1060$ m) parts of the basin at GL-6 m. The choice for these locations inside the basin is made based on the results of Section 3.3.2. The first location corresponds to the basin margin, and the second location to the centre of the basin. The sediment-bedrock interface is defined at GL-27.35 m and GL-225 m for the first and second locations, respectively. The input motion is as shown in Fig. 3.

Time histories of acceleration (top panel), velocity (middle panel) and displacement (bottom panel) for the left section (left-hand panels) and the central section (right-hand panels) are compared between the 1-D and 1-D models in Fig. 14. Beyond 2 seconds of wave propagation, motion is seen to be attenuated in 1-D, while the SH waves inside the 1-D basin still propagate until the end of the simulation. Our additional tests on 1-D and 1-D models indicate that the 1-D geometry results in an amplified and extended wave propagation within the basin (at both locations) in the linear case (see Supplementary Appendix C). The wave propagation in 1-D remains complex compared to 1-D, also when considering the soil non-linearity, as illustrated by the continuous reflections and the amplitude differences between the 1-D and 1-D results. The strongest motion is at 1.5 s, and the PGA at both sections is greater in 1-D than in 1-D (approximately 1.5 m s^{-2} in 1-D; 2 m s^{-2} in 1-D at the left section and slightly weaker in the centre of the basin). In displacement-time histories, longer durations of ground motion are observed in the 1-D model in both sections, while the strongest displacement is damped after the first peak in 1-D. This aspect is seen clearly in the centre of the basin.

Fig. 15 displays the comparison of the 1-D and 1-D Fourier amplitudes of the surface velocities for the two locations. The signal content in the left section displays a resonance peak at around 3 Hz, attributed to the thin sedimentary layer resonance. The frequency content of the 1-D motion at the same section is slightly shifted towards higher frequencies with consistently higher fundamental resonance frequencies in this 1-D model than in the corresponding 1-D model (see the discussion in Section 3.3.1). In the central section, the shape of the Fourier amplitudes of the 1-D and 1-D approaches are similar. However, 1-D amplification is slightly shifted

Downloaded from https://academic.oup.com/gji/article-abstract/217/2/1353/5298487 by guest on 09 April 2019

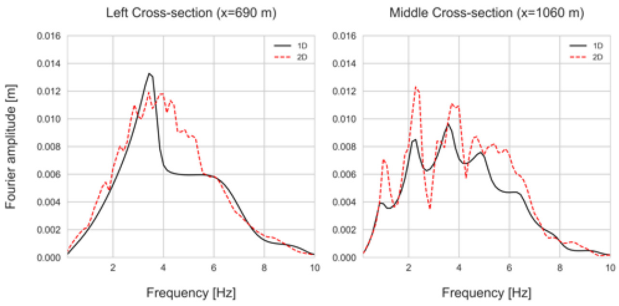

Figure 15. Comparison of Fourier amplitudes of the surface velocities between 1-D (solid lines) and 1-D (dashed lines) approaches for the left column (left-hand panel) and central column (right-hand panel) of the basin model for non-linearity with pore-pressure effects.

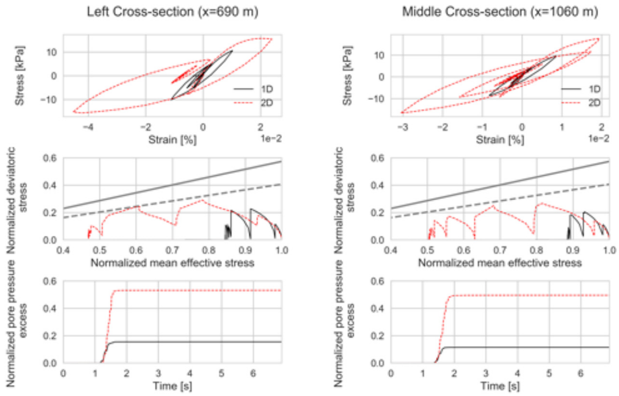

Figure 16. Comparison of stress–strain curves (top panel), deviatoric plan (middle panel) and temporal change of pore-pressure excess (bottom panel) between 1-D (solid lines) and 1-D (dashed lines) approaches for the left column (left-hand panel) and central column (right-hand panel) for non-linearity with pore-pressure effects. Failure and phase transformation lines are indicated by grey solid and dashed lines (in grey), respectively, in the deviatoric plans shown in the middle panels.

towards higher frequencies compared to that in 1-D. The wave propagation in the 1-D model produces significant amplification over the whole frequency band.

To compare the non-linearity levels of 1-D and 1-D models, we further analyse the stress–strain curves, deviatoric plan and excess-pore pressure development. Fig. 16 displays this comparison for the left location (left-hand panel) and the central location (right-hand panel) inside the basin. Deviatoric plan quantifies the change in effective stress of liquefiable soil under applied shearing. Deviatoric stress and effective stress values are normalized by the initial effective mean stress. This normalization is also applied to pore-pressure excess values. In the stress–strain diagram of the left column, soil experiences approximately 4.5 times larger deformation in the 1-D model (0.045 per cent) than in the 1-D model (0.01 per cent). For the central column, a similar difference is seen between the 1-D and 1-D models with slightly lower values of strain (approximately four times more strain in 1-D than 1-D). Higher strength loss is apparent from the lower stress–strain tangent in the 1-D results of both sections, as compared to 1-D. These results indicate that the level of non-linearity triggered in the 1-D model is higher than in 1-D. The amplifications of ground motion in the 1-D model enhance the basin non-linearity. The increase in non-linearity is also seen in the decrease of effective stress values. In both sections, the initial soil strength is reduced to its half in the 1-D model, whereas it is limited to a decrease of 15 and 10 per cent for the left and central sections, respectively, in the 1-D model. Such a decrease in effective stress values results from the rise of pore-pressure excess. The 1-D soil non-linearity is shown to induce excess-pore pressure development of more than 50 per cent at both columns. Soil non-linearity is relatively low in 1-D so that the pore-pressure excess is less than 15 per cent at both sections. We note that the complex wave propagation triggers more non-linearity and accordingly enhances the pore-pressure level in the 1-D model compared to the 1-D case.

These results demonstrate that the combined effect of the 1-D geometry and the soil non-linearity results in a more complex wave propagation in 1-D as compared to 1-D. Higher wave amplitudes and extended wave propagation due to the 1-D effects enhance the pore-pressure excess and trigger additional non-linearity. This effect of the dimensionality on non-linear basin response is clearly seen even though the maximum strain is only modest (<0.1 per cent). On the other hand, Fourier spectra, and therefore amplification functions with respect to the linear bedrock, are still higher in 1-D than in 1-D in some frequency bands. Thus, taking into account the 1-D-geometry effects has great importance for modelling seismic wave propagation both in linear and non-linear media.

4 CONCLUSIONS AND PERSPECTIVES

The 1-D-3C spectral element modelling in Oral *et al.* (2017) has been extended to 1-D for modelling the non-linear soil response with pore-pressure effects in multidimensional media. The MPII model of Iwan (1967) and liquefaction front model of Iai *et al.* (1990) are implemented to SEM2DPACK software, and verification of the implementation of new features is performed. The code is suitable for studying the effects of various physical processes, such as attenuation and non-linear material behaviour including pore-pressure effects on the ground motion.

The extended numerical model has been applied to a 2-D sedimentary basin model to study the effect of soil non-linearity on wave propagation in complex media. The 1-D basin model consists of six soft layers situated within a basin surrounded by bedrock. Basin and bedrock are separated on one side by an elliptical boundary and on the other side by a boundary with a steeper inclination, introducing complexity in the wave propagation in the model owing to the asymmetry of the basin geometry. Two superficial soil layers are dictated to be susceptible to excess-pore pressure development, and we performed non-linear analyses with and without pore-pressure effects using a truncated Gaussian signal with a free surface PGA of 0.20 g in the in-plane (P-SV) and out-of-plane (SH) wave propagation models. We found that:

(1) Non-linear basin response is sensitive to the differences in P-SV and SH waves propagation. As expected, the 1-D basin geometry results in interference of basin-edge generated waves and vertically propagating waves and, hence induces differences in P-SV and SH wave propagation. The basin response in the P-SV and SH models remains different also under non-linear effects.

(2) The excess-pore pressure development in shallow layers triggers more non-linearity, and it causes additional strength loss and deformation in these layers. Therefore, pore-pressure effects increase the strain contrast between superficial layers and the rest of the basin. Moreover, the asymmetric basin geometry results in spatial variability of such non-linear effect: patches with relatively high strain values in shallow layers are computed, in particular at the centre of the basin and close to basin margins.

Downloaded from https://academic.oup.com/gji/article-abstract/217/2/1353/5298487 by guest on 09 April 2019

(3) The energy of ground motion is damped in the whole frequency band (at frequencies below 8 Hz where the energy content of the source is relatively high) when considering non-linearity without pore-pressure effects. Some of the past studies point to the amplification of low-frequency content of surface motion due to significant excess-pore pressure development (e.g. Laurendeau *et al.* 2017; Oral *et al.* 2017). Yet, such notable pore-pressure related effects are not found in surface motion (such as time histories of acceleration, velocity and displacement) in this case where a simple wavelet is used as input motion. Exploring this aspect under different input motion needs further study. Studying the changes in triggered non-linearity level under realistic input motion with a complex energy content is a critical topic for future investigations.

(4) As already known for linear soil response, the 1-D basin geometry results in amplification of wave amplitudes and increase of duration of wave propagation with respect to 1-D. A complex wave propagation in 1-D modelling brings higher non-linearity all over the basin compared to 1-D modelling. High degrees of non-linearity in 1-D modelling could lead to strength loss and pore-pressure rise that cannot be predicted from 1-D modelling. Furthermore, amplification functions with respect to the linear bedrock are still higher in 1-D than in 1-D in some frequency bands. Thus, we recommend multidimensional modelling of wave propagation in seismic hazard assessment studies for non-linear complex media.

This numerical study aims at better understanding the physics and the key parameters governing the 1-D non-linear wave propagation. Our results highlight the importance of considering 1-D geometry and soil non-linearity and are stable for different soil conditions (as verified after a sensitivity study on the effect of liquefaction-related parameters). One can expect similar results for comparison of 1-D versus 3-D modelling. Moreover, we recall that the source in this study is defined as a vertically incident wavefield, which is warranted under the assumption that the model domain is positioned sufficiently far from fault, that is for far-field ground-motion modelling. In the near-field region, source properties and its rupture process become significant factors to account for in seismic hazard studies. Certain studies successfully model 3-D near-field ground motion including the causative fault itself assuming linear media or non-linear media for a limited frequency band (e.g. Stupazzini *et al.* 2009; Oral *et al.* 2018). Improving the knowledge of non-linear effects on ground motion under rather simplified conditions of input and geometry (1-D versus 3-D), as scoped in this study, is helpful prior to real case scenarios (such as studying near-field broad-band ground-motion in 3-D non-linear media). In that sense, our study constitutes a sensitivity analysis preliminary to comprehensive real-case studies. The extension of our analyses on a real basin and also considering near-field input conditions are future perspectives.

DATA AND RESOURCES

The numerical tool for 1-D spectral-element wave propagation modelling (version 2.3.8) is available at https://github.com/jpampuero/sem2dpack address. All the updates can be followed on the same address.

ACKNOWLEDGEMENTS

The authors would like to thank Harsha S. Bhat, Jean-Paul Ampuero and Marion Thomas for their collaboration and helpful comments in using SEM2DPACK for multidimensional modelling of seismic wave propagation in non-linear media, to Elise Delavaud for her assistance in the preparation of this work, and to Martijn van den Ende for his final touch to enrich the readability of the manuscript.

We furthermore acknowledge the comments of the Editor René-Edouard Plessix and two anonymous reviewers, which definitely improved the quality of the manuscript.

REFERENCES

Aguirre, J. & Irikura, K., 1997. Nonlinearity, liquefaction, and velocity variation of soft soil layers in Port Island, Kobe, during the Hyogo-Ken Nanbu Earthquake, *Bull. seism. Soc. Am.,* **87,** 1244–1258.

Ampuero, J.-P., 2002, Etude physique et numérique de la nucléation des séismes, *PhD thesis*, Paris 7.

Assimaki, D., Li, W. & Kalos, A., 2011. A wavelet-based seismogram inversion algorithm for the in-situ characterization, *Pure appl. Geophys.,* **168**(10), 1669–1691.

Bakir, B.S., Sucuoglu, H. & Yilmaz, T., 2002. An overview of local site effects and the associated building damage in Adapazari during the 17 August 1999 Izmit Earthquake, *Bull. seism. Soc. Am.,* **92**(1), 509–526.

Bard, P.-Y. & Bouchon, M., 1985. The two-dimensional resonance of sediment-filled valleys, *Bull. seism. Soc. Am.,* **75**(2), 519–541.

Bonilla, L.F., Archuleta, R.J. &Lavallée, 2005. Hysteretic and dilatant behavior of cohesionless soils and their effects on nonlinear site response: field data observations and modeling, *Bull. seism. Soc. Am.,* **95**(6), 2373–2395.

Bonilla, L.F., Liu, P.-C. & Nielsen, S., 2006. 1-D and 2D linear and nonlinear site response in the grenoble area, in *Proceedings of the 3rd International Symposium on the Effects of Surface Geology on Seismic Motion (ESG2006),* Grenoble, France.

Bonilla, L.F., Tsuda, K., Régnier, J. & Laurendeau, A., 2011. Nonlinear site response evidence of k-net and kik-net records from the 2011 off the Pacific coast of Tohoku Earthquake, *Earth, Planets Space,* **63**(7), 785–789.

Bradley, B.A. & Cubrinovski, M., 2011. Near-source strong ground motions observed in the 22 February 2011 Christchurch Earthquake, *Seismol. Res. Lett.,* **82**(6), 853–865.

Campillo, M., Gariel, J., Aki, K. & Sanchez-Sesma, F., 1989. Destructive strong ground motion in Mexico City: source, path, and site effects during great 1985 Michoacán Earthquake, *Bull. seism. Soc. Am.,* **79**(6), 1718–1735.

Chávez-García, F.J. & Bard, P.-Y., 1994. Site effects in mexico city eight years after the September 1985 Michoacan Earthquakes, *Soil Dyn. Earthq. Eng.,* **13**(4), 229–247.

Chiaro, G., Kiyota, T., Pokhrel, R.M., Goda, K., Katagiri, T. & Sharma, K., 2015. Reconnaissance report on geotechnical and structural damage caused by the 2015 Gorkha Earthquake, Nepal, *Soils Found.,* **55**(5), 1030–1043.

Darendeli, M.B., 2001, Development of a new family of normalized modulus reduction and material damping curves, *PhD thesis*, The University of Texas at Austin.

Delavaud, E., 2007. Simulation numérique de la propagation d'ondes en milieu géologique complexe: application à l'évaluation de la réponse sismique du bassin de Caracas (Venezuela), *PhD thesis*, Institut de Physique du Globe de Paris.

Delavaud, E., Cupillard, P., Festa, G. & Vilotte, J.-P., 2006. 3d spectral element method simulations of the seismic response in the Caracas Basin, in *Proceedings of the Third International Symposium on the Effects of Surface Geology on Seismic Motion,* pp. 515–522, Grenoble.

Dupros, F., De Martin, F., Foerster, E., Komatitsch, D. & Roman, J., 2010. High-performance finite-element simulations of seismic wave propagation in three-dimensional nonlinear inelastic geological media, *Parallel Comput.,* **36**(5), 308–325.

Electric Power Research Institute, E., 1993. Guidelines for determining design basis ground motions, Tech. rep., Electric Power Reasearch Institute Technological Report EPRI TR-102293.

Downloaded from https://academic.oup.com/gji/article-abstract/217/2/1353/5298487 by guest on 09 April 2019

Ermert, L., Poggi, V., Burjánek, J. & Fäh, D., 2014. Fundamental and higher two-dimensional resonance modes of an Alpine Valley, *Geophys. J. Int.,* **198**(2), 795–811.

Faccioli, E., Maggio, F., Paolucci, R. & Quarteroni, A., 1997. 2D and 3D elastic wave propagation by a pseudo-spectral domain decomposition method, *Journal of Seismology,* **1**(3), 237–251.

Festa, G. & Vilotte, J.P., 2005. The newmark scheme as velocity–stress time-staggering: an efficient PML implementation for spectral element simulations of elastodynamics, *Geophys. J. Int.,* **161**(3), 789–812.

Gandomzadeh, A., 2011. Dynamical soil-structure interactions: influence of soil behaviour nonlinearities, *PhD thesis*, Université Paris-Est.

Gélis, C. & Bonilla, L.F., 2012. 2-dp-sv numerical study of soil-source interaction in a non-linear basin, *Geophys. J. Int.,* **191**(3), 1374–1390.

Gélis, C. & Bonilla, L.F., 2014. Influence of a sedimentary basin infilling description on the 2-D P-SV wave propagation using linear and non-linear constitutive models, *Geophys. J. Int.,* **198**(3), 1684–1700.

Guidotti, R., Stupazzini, M., Smerzini, C., Paolucci, R. & Ramieri, P., 2011. Numerical study on the role of basin geometry and kinematic seismic source in 3d ground motion simulation of the 22 February 2011 mw 6.2 Christchurch earthquake, *Seismol. Res. Lett.,* **82**(6), 767–782.

Haney, M., Snieder, R., Ampuero, J.-P. & Hofmann, R., 2007. Spectral element modelling of fault-plane reflections arising from fluid pressure distributions, *Geophys. J. Int.,* **170**(2), 933–951.

Hardin, B.O. & Drnevich, V.P., 1972. Shear modulus and damping in soils: measurement and parameter effects, *J. Soil Mech. Found. Div,* **98**(sm6).

Iai, S., Matsunaga, Y. & Kameoka, T., 1990. Strain space plasticity model for cyclic mobility, *Rep. Port Harbour Res. Inst.,* **29,** 57–83.

Iai, S., Morita, T., Kameoka, T., Matsunaga, Y. & Abiko, K., 1995. Response of a dense sand deposit during 1993 Kushiro-Oki earthquake, *Soils Found.,* **35**(1), 115–131.

Ishibashi, M.P. & Zhang, X., 1993. Unified dynamic shear moduli and damping patios of sand and clay, *Soils Found.,* **33**(1), 182–191.

Iwan, W.D., 1967. On a class of models for the yielding behavior of continuous and composite systems, *J. Appl. Mech.,* **34**(3), 612–617.

Joyner, W.B., 1975. A method for calculating nonlinear seismic response in two dimensions, *Bull. seism. Soc. Am.,* **65**(5), 1337–1357.

Kawase, H. & Aki, K., 1989. A study on the response of a soft basin for incident S, P, and Rayleigh waves with special reference to the long duration observed in mexico city, *Bull. seism. Soc. Am.,* **79**(5), 1361–1382.

Komatitsch, D. & Vilotte, J.P., 1998. The spectral element method: an efficient tool to simulate the seismic response of 2D and 3D geological structures, *Bull. seism. Soc. Am.,* **88**(2), 368–392.

Lacave, C. & Lemeille, F., 2006. Seismic hazard and Alpine Valley response analysis: generic valley configurations, in *Proceedings of the Third International Symposium on the Effects Of Surface Geology on Seismic Motion,* Grenoble, France, p. 1.

Laurendeau, A. *et al.*, 2017. Low-frequency seismic amplification in the Quito Basin (Ecuador) revealed by accelerometric recordings of the renac network, *Bull. seism. Soc. Am.,* **107**(6), 2917–2926.

Liu, P. & Archuleta, R.J., 2006. Efficient modeling of q for 3D numerical simulation of wave propagation, *Bull. seism. Soc. Am.,* **96**(4A), 1352–1358.

Lyakhovsky, V. & Hamiel, Y., 2009. Nonlinear elasticity and scalar damage rheology model for fractured rocks, in *Meso-Scale Shear Physics in Earthquake and Landslide Mechanics,* CRC Press, pp. 123–132.

Madariaga, R., Ampuero, J. & Adda-Bedia, M., 2006. Seismic radiation from simple models of earthquakes, *Earthquakes: Radiated Energy and the Physics of Faulting,* pp. 223–236.

Martino, S., Lenti, L., Gélis, C., Giacomi, A.C., Santisi d'Avila, M., Bonilla, L.F., Bozzano, F. & Semblat, J.F., 2015. Influence of lateral heterogeneities on strong-motion shear strains: simulations in the historical center of Rome (Italy), *Bull. seism. Soc. Am.,* **105**(5), 2604–2624.

Maufroy, E. *et al.*, 2015. Earthquake ground motion in the mygdonian basin, Greece: the e2vp verification and validation of 3D numerical simulation up to 4 hz, *Bull. seism. Soc. Am.*

O'Brien, G.S. & Bean, C.J., 2011. An irregular lattice method for elastic wave propagation, *Geophys. J. Int.,* **187**(3), 1699–1707.

Olsen, K.B. & Archuleta, R.J., 1996. Three-dimensional simulation of earthquakes on the Los Angeles fault system, *Bull. seism. Soc. Am.,* **86**(3), 575–596.

Oral, E., 2016. Modélisation de la propagation des ondes sismiques dans les milieux linéaires et non-linéaires, *PhD thesis*, Université Paris-Est.

Oral, E., Gélis, C., Bonilla, L.F. & Delavaud, E., 2017. Spectral element modelling of seismic wave propagation in visco-elastoplastic media including excess-pore pressure development, *Geophys. J. Int.,* **211**(3), 1494–1508.

Oral, E., Lopez-Caballero, F. & Gatti, F., 2018. 3d spectral element modeling of near source effects including kinematic rupture and finite-fault effects, in *Proceedings of the 16th European Conference on Earthquake Engineering,* Thessaloniki, Greece.

Peyrusse, F., Glinsky, N., Gélis, C. & Lanteri, S., 2014. A high-order discontinuous Galerkin method for viscoelastic wave propagation, in *Spectral and High Order Methods for Partial Differential Equations-ICOSAHOM 2012,* pp. 361–371, Springer.

Pham, V.A., 2013. Effets de la pression interstitielle sur la reponse sismique des sols: modélisation numérique 1-D/ 3 composantes, *PhD thesis*, Université Paris-Est.

Priolo, E. & Seriani, G., 1993. Spectral element method with substructuring: an accurate and efficient high-order finite element approach for wave modeling, *Environ. Acoust., Scatter. Propag.,* **2,** 509–527.

Roten, D., Fäh, D., Cornou, C. & Giardini, D., 2006. Two-dimensional resonances in alpine valleys identified from ambient vibration wavefields, *Geophys. J. Int.,* **165**(3), 889–905.

Roten, D., Olsen, K. & Pechmann, J., 2012. 3d simulations of m 7 earthquakes on the wasatch fault, Utah, part II: broadband (0–10 Hz) ground motions and nonlinear soil behavior, *Bull. seism. Soc. Am.,* **102**(5), 2008–2030.

Roten, D., Fäh, D. & Bonilla, L.F., 2013. High-frequency ground motion amplification during the 2011 Tohoku earthquake explained by soil dilatancy, *Geophys. J. Int.,* **193**(2), 898–904.

Roten, D., Fäh, D. & Bonilla, L.F., 2014. Quantification of cyclic mobility parameters in liquefiable soils from inversion of vertical array records, *Bull. seism. Soc. Am.,* **104**(6), 3115–3138.

Sánchez-Sesma, F.J., 1985. Diffraction of elastic sh waves by wedges, *Bull. seism. Soc. Am.,* **75**(5), 1435–1446.

Semblat, J.F., Kham, M., Parara, E., Bard, P.-Y., Pitilakis, K., Makra, K. & Raptakis, D., 2005. Seismic wave amplification: basin geometry vs soil layering, *Soil Dyn. Earthq. Eng.,* **25**(7-10), 529–538.

Seriani, G. & Priolo, E., 1991. High-order spectral element method for acoustic wave modeling, in *SEG Technical Program Expanded Abstracts 1991,* 1561–1564

Smerzini, C., Paolucci, R. & Stupazzini, M., 2011. Comparison of 3D, 2D and 1-D numerical approaches to predict long period earthquake ground motion in the gubbio plain, Central Italy, *Bull. Earthq. Eng.,* **9**(6), 2007–2029.

Smith, S. & Snieder, R., 2010. Seismic modeling and analysis of a prototype heated nuclear waste storage Tunnel, Yucca Mountain, Nevada, *Geophysics,* **75**(1), T1–T8.

Stacey, R., 1988. Improved transparent boundary formulations for the elastic-wave equation, *Bull. seism. Soc. Am.,* **78**(6), 2089–2097.

Stupazzini, M., Paolucci, R. & Igel, H., 2009. Near-fault earthquake ground-motion simulation in the grenoble valley by a high-performance spectral element code, *Bull. seism. Soc. Am.,* **99**(1), 286–301.

Takemiya, H. & Adam, M., 1998. 2d nonlinear seismic ground analysis by FEM BEM: the case of kobe in the Hyogo-ken Nanbu earthquake, *Struct. Eng. Earthq. Eng.,* **15,** 19s–28s.

Tokimatsu, K., Mizuno, H. & Kakurai, M., 1996. Building damage associated with geotechnical problems, *Soils Found.,* **36**(Special), 219–234.

Vucetic, M. & Dobry, R., 1991. Effect of soil plasticity on cyclic response, *J. Geotech. Eng.,* **117**(1), 89–107.

Downloaded from https://academic.oup.com/gji/article-abstract/217/2/1353/5298487 by guest on 09 April 2019

SUPPORTING INFORMATION

Supplementary data are available at *GJI* online.

Figure S1. GOF between the reference solution (1-D) and the 1-D solution on the computed velocity-time histories for Volvi model. It is shown the frequency envelope goodness FEG (left-hand panel), time-frequency envelope goodness TFEG (right-hand panel), time envelope goodness TEG (middle right-hand panel) (top panel) and frequency phase goodness FPG (left-hand panel), time-frequency phase goodness TFPG (right-hand panel) and time phase goodness TPG (middle right-hand panel) (bottom panel).

Figure S2. Spectral-ratio distribution of the viscoelastic surface motion for horizontal component of P-SV model of Gélis & Bonilla (2014) (left-hand panel) and P-SV model of our study (right-hand panel) on the frequency band 0.2–10 Hz.

Figure S3. Spectral-ratio distribution of the viscoelastic surface motion for horizontal component of SH model of Gélis & Bonilla (2014) (left-hand panel) and SH model of our study (right-hand panel) on the frequency band 0.2–10 Hz.

Figure S4. Comparison of time histories of surface velocity in horizontal direction (left-hand panel) and comparison of stress–strain curves at GL-10 m (right-hand panel) for 1-D (in blue) and 1-D (in red) SEM codes for stress-independent non-linear P1 model under uniaxial loading.

Figure S5. GOF between the reference solution (1-D) and the 1-D solution on the computed velocity-time histories for P1 model. It is shown the frequency envelope goodness FEG (left-hand panel), time–frequency envelope goodness TFEG (right-hand panel), time envelope goodness TEG (middle right-hand panel) (top panel) and frequency phase goodness FPG (left-hand panel), time-frequency phase goodness TFPG (right-hand panel) and time phase goodness TPG (middle right-hand panel) (bottom panel).

Figure S6. Surface-velocity time histories in NS and UD directions (left-hand panel) and stress–strain curves at GL-4 m (right-hand panel) for 1-D (in blue) and 1-D (in red) SEM solutions of WRLA model.

Figure S7. GOF between the reference solution (1-D) and the 1-D solution on the computed velocity-time histories for WRLA model. It is shown the frequency envelope goodness FEG (left-hand panel), time-frequency envelope goodness TFEG (right-hand panel), time envelope goodness TEG (middle right-hand panel) (top panel) and frequency phase goodness FPG (left-hand panel), time-frequency phase goodness TFPG (right-hand panel) and time phase goodness TPG (middle right-hand panel) (bottom panel).

Figure S8. Stress–strain curves (in red) with backbone curve (in black) (left-hand panel), applied stress as a function of number of loading cycles (right-hand panel) (top panel), change of axial strain as a function of number of loading cycles (left-hand panel) and and deviatoric plan (right-hand panel) (bottom panel) for the mid-layer 2 when CSR is 0.2.

Figure S9. Liquefaction resistance curves for layers 1 (solid line) and 2 (dashed line) for case 1 (in black) and case 2 (in red).

Figure S10. Spectral-ratio distribution of the surface-motion for horizontal component of P-SV model (top panel) and SH model (bottom panel) for viscoelasticity (left-hand panel), non-linearity model without pore-pressure effects (total stress analysis) (middle) and non-linearity model with pore-pressure effects (effective stress analysis) (right-hand panel) for case 2.

Figure S11. Spectral-ratio distribution of the surface-motion for horizontal component of P-SV model (top panel) and SH model (bottom panel) for viscoelasticity (left-hand panel), non-linearity model without pore-pressure effects (total stress analysis) (middle panel) and non-linearity model with pore-pressure effects (effective stress analysis) (right-hand panel) for case 3.

Figure S12. Maximum-strain (top panel) and trigger-time (bottom panel) distribution of P-SV model (left-hand panel) and SH model (right-hand panel) for non-linearity with pore-pressure effects for case 2. Localization of maximal values is shown with a star.

Figure S13. Maximum-strain (top panel) and trigger-time (bottom panel) distribution of P-SV model (left-hand panel) and SH model (right-hand panel) for non-linearity with pore-pressure effects for case 3. Localization of maximal values is shown with a star.

Figure S14. Comparison of stress–strain curves at GL-3.5 m (top panel) and GL-11.5 m (bottom panel) (left-hand panel) and comparison of time histories of surface-acceleration (top panel), velocity (middle panel) and displacement (bottom panel) between effective (in dashed line) and total (in solid line) stress analyses in P-SV model for case 2.

Figure S15. Comparison of stress–strain curves at GL-3.5 m (top panel) and GL-11.5 m (bottom panel) (left-hand panel) and comparison of time histories of surface-acceleration (top panel), velocity (middle panel) and displacement (bottom panel) between effective (in dashed line) and total (in solid line) stress analyses in SH model for case 2.

Figure S16. Comparison of stress–strain curves at GL-3.5 m (top panel) and GL-11.5 m (bottom panel) (left-hand panel) and comparison of time histories of surface-acceleration (top panel), velocity (middle panel) and displacement (bottom panel) between effective (in dashed line) and total (in solid line) stress analyses in P-SV model for case 3.

Figure S17. Comparison of stress–strain curves at GL-3.5 m (top panel) and GL-11.5 m (bottom panel) (left-hand panel) and comparison of time histories of surface-acceleration (top panel), velocity (middle panel) and displacement (bottom panel) between effective (in dashed line) and total (in solid line) stress analyses in SH model for case 3.

Figure S18. Comparison of time histories of surface acceleration (top panel), velocity (middle panel) and displacement (bottom panel) between 1-D (in solid line) and 1-D (in dashed line) approaches for left column (left-hand panel) and middle column (right-hand panel) for linear case.

Figure S19. Comparison of Fourier amplitudes of surface velocities between 1-D (in solid line) and 1-D (in dashed line) approaches for left column (left-hand panel) and middle column (right-hand panel) of the basin model for linear case.

Figure S20. Comparison of time histories of surface acceleration (top panel), velocity (middle panel) and displacement (bottom panel) between linear (in solid line) and non-linear (in dashed line) approaches for left column (left-hand panel) and middle column (right-hand panel) for 1-D case.

Figure S21. Comparison of Fourier amplitudes of surface velocities between linear (in solid line) and non-linear (in dashed line) approaches for left column (left-hand panel) and middle column (right-hand panel) of the basin model for 1-D case.

Figure S22. Comparison of time histories of surface acceleration (top panel), velocity (middle panel) and displacement (bottom panel) between linear (in solid line) and non-linear (in dashed line) approaches for left column (left-hand panel) and middle column (right-hand panel) for 1-D case.

Figure S23. Comparison of Fourier amplitudes of surface velocities between linear (in solid line) and non-linear (in dashed line)

Downloaded from https://academic.oup.com/gji/article-abstract/217/2/1353/5298487 by guest on 09 April 2019

approaches for left column (left-hand panel) and middle column (right-hand panel) of the basin model for 1-D case.

Please note: Oxford University Press is not responsible for the content or functionality of any supporting materials supplied by the authors. Any queries (other than missing material) should be directed to the corresponding author for the paper.

Downloaded from https://academic.oup.com/gji/article-abstract/217/2/1353/5298487 by guest on 09 April 2019